

Fault Identification of Rotating Machinery Based on Dynamic Feature Reconstruction Signal Graph

Wenbin He, Jianxu Mao, Zhe Li, *Member, IEEE*, Yaonan Wang, Qiu Fang, *Member, IEEE*, and Haotian Wu

Abstract—To improve the performance in identifying the faults under strong noise for rotating machinery, this paper presents a dynamic feature reconstruction signal graph method, which plays the key role of the proposed end-to-end fault diagnosis model. Specifically, the original mechanical signal is first decomposed by wavelet packet decomposition (WPD) to obtain multiple sub-bands including coefficient matrix. Then, with originally defined two feature extraction factors MDD and DDD, a dynamic feature selection method based on L2 energy norm (DFSL) is proposed, which can dynamically select the feature coefficient matrix of WPD based on the difference in the distribution of norm energy, enabling each sub-signal to take adaptive signal reconstruction. Next the coefficient matrices of the optimal feature sub-bands are reconstructed and reorganized to obtain the feature signal graphs. Finally, deep features are extracted from the feature signal graphs by 2D-Convolutional neural network (2D-CNN). Experimental results on a public data platform of a bearing and our laboratory platform of robot grinding show that this method is better than the existing methods under different noise intensities.

Index Terms—Fault identification, wavelet packet, dynamic feature selection, feature signal graph, 2D-Convolutional neural network.

I. INTRODUCTION

ROTATING machinery is widely used in industrial sites, aerospace, marine ships, rail transit and other large-scale equipments [1], [2]. It usually works under harsh working conditions where a small fault may produce a chain reaction leading to catastrophic system failure. It is of great significance to diagnose the faults of rotating machinery accurately as early as possible [3]. Generally speaking, fault diagnosis methods can be divided into two categories: 1) model-based methods and 2) data-based methods. In the era of Internet of Things and big data, data-based methods provide a new idea for end-to-end fault diagnosis, so efficient intelligent fault diagnosis based on data collected by sensors is a research focus of reliability monitoring of rotating machinery [4]. They are defined from the perspective of pattern recognition and

This work was supported in part by the National Key Research and Development Program of China under Grant 2020YFB1712600; in part by the National Natural Science Foundation of China under Grant 62133005, Grant 61903134, Grant 62293510/62293512, Grant 62293510/62293515, Grant 62027810; in part by the Special funding support for the construction of innovative provinces in Hunan Province under Grant 2021GK1010; and in part by China Postdoctoral Science Foundation under Grant 2022M721097. (Corresponding author: Zhe Li)

Wenbin He, Jianxu Mao, Zhe Li, Yaonan Wang, Qiu Fang, and Haotian Wu are with the College of Electrical and Information Engineering and the National Engineering Research Center of Robot Visual Perception and Control Technology, Hunan University, Changsha 410082, China. (email: hwenbin@hnu.edu.cn; maojianxu@hnu.edu.cn; zheli@hnu.edu.cn; yaonan@hnu.edu.cn; qfang@hnu.edu.cn; wuhaotian@hnu.edu.cn)

include three steps: 1) data collection; 2) feature extraction; and 3) fault classification [5]. Many researchers analyzed sensor signals and identified faults based on various methods, including time domain analysis, frequency spectrum analysis, wavelet transform analysis and time-frequency analysis. At the same time, thanks to the rapid development of deep learning technology, many signal feature extraction methods based on deep learning have been proposed [6]–[10]. In particular, the powerful feature extraction capability of CNN has made great success in the field of fault diagnosis. Xu and Wang developed fault diagnosis algorithms with good robustness to noise signals based on CNN [11], [12]. Under the framework of CNN, Chen et al. [13] combined channel attention mechanism, spatial attention mechanism and residual structure to improve the accuracy of traditional deep network in fault diagnosis tasks. Huang et al. [14], [15] combined CNN and Long Short Term Memory (LSTM) to improve the prediction accuracy of fault diagnosis. In literature [16], Jin et.al proposed an improved fault diagnosis method based on CNN for rotating machineries, called the LiNet, which can achieve nearly 100% accuracy under clean signal.

However, the working conditions and transmission systems of rotating machinery are very complex and diverse, the signals generated are nonlinear and non-stationary. The signals generated by various excitation sources are fuzzy, mixed and multi-coupled. Bearing impact failure characteristics are often submerged in strong background signal noise and difficult to identify [17]. Therefore, how to identify faults from noise is of great significance to practical engineering problems. Some methods have been tried to solve this problem. For example: Shao et al. [18] realized the fault diagnosis of rotating machinery with signal-to-noise ratio (SNR) of 12-24dB by using a modified stacked auto-encoder (MSAE). The hybrid robust convolutional autoencoder (HRCAE) fault diagnosis method proposed by Yan et al. can effectively suppress the influence of noise for computer numerical control (CNC) machine tools [19]. The fault diagnosis model based on multi-source data fusion and deep residual neural network proposed by Peng et al. can achieve 99% recognition rate when $\text{SNR} \geq 6\text{dB}$ [20]. Hu et al. [21] proposed a new intelligent fault diagnosis approach based on tensor-aligned invariant subspace learning and two-dimensional convolutional neural networks for cross-domain intelligent fault diagnosis of bearings. It realized high-precision cross domain fault diagnosis under the condition of noise ratio of 0% to 20% ($\text{SNR} \geq 7\text{dB}$). In [5], the ResNet-APReLU method is proved to achieve good accuracy and stability when SNR is 5dB-1dB.

Most of the fault diagnosis models developed by above

researchers are based on signals without noise or under weak noise pollution, while the other part of researchers used signals with a certain SNR to verify the robustness of the proposed fault diagnosis model. Unfortunately, in the practical industrial scene, basically, there is no clean signal [22]. Therefore, this paper focuses on the problem of fault identification under strong noise. A fault identification algorithm based on wavelet packet dynamic reconstructed feature signal graph and 2D-CNN (WPDRG-2DCNN) is developed. Each signal is processed by adaptive feature coefficient selection and signal reconstruction, and the signal feature graph layer is introduced into hierarchical CNN. The feature coefficient matrix of WPD is dynamically selected based on the distribution difference of norm energy, enabling adaptive signal reconstruction for each sub-signal, thereby optimizing the global feature extraction capability of CNN and improving fault identification performance.

The main contributions of this article are as follows:

- 1) Aiming at the fault identification of rotating machinery in the scene under strong industrial noise, a new fault diagnosis approach WPDRG-2DCNN is proposed. This approach can transform the original mechanical signal into feature signal graphs, and extract the deep fault information from the feature graphs.
- 2) Two feature extraction factors MDD and DDD are defined, which are used to adjust the feature energy distribution and thus control the global and local feature extraction, respectively.
- 3) A dynamic feature selection method based on L2 energy norm, that is, DFSL, is proposed. The method can select the optimal feature sub-bands from each sub-signal adaptively according to the difference and distribution of energy.
- 4) Ablation experiments and comparison experiments with advanced methods were carried out on the public data set and the real data set of our laboratory. The experimental results show that the proposed method is better than the existing methods in fault identification under different strong noises.

The rest of this article is organized as follows. Section II introduces the theoretical support of the proposed method. Section III introduces the application of the proposed WPDRG-2DCNN method in fault identification. Section IV describes the experimental analysis, the experiment is based on the public data set of bearing and the data collected by the robot grinding platform in our laboratory. Finally, Section V concludes this article and looks forward to the future.

II. METHODOLOGY

A. WPD

For any given discrete signal $x(i) \in L^2(R)$, discrete dyadic wavelet transform is defined as the inner product of wavelet function and signal

$$C(j, n) = \sum_{i \in Z} x(i) \psi_{j,n}(i) \quad (1)$$

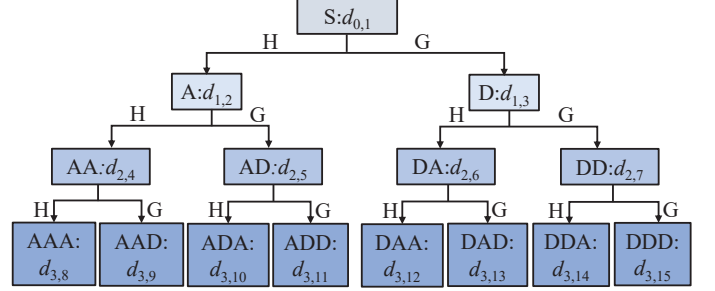


Fig. 1. Three-level WPD for a given signal.

where $\psi_{j,n}(i)$ is the discrete dyadic wavelet function at scale j and position i , i.e.

$$\psi_{j,n}(i) = 2^{-j/2} \psi(2^{-j}(i-n)) \quad (2)$$

The signal $x(i)$ can be reconstructed by using wavelet functions and wavelet coefficients:

$$x(i) = \sum_j \sum_n C(j, n) \psi_{j,n}(i). \quad (3)$$

WPD is an extension of discrete wavelet transform, which can further decompose the details of signal in high frequency region [23]. Thus, WPD can better analyze signals in time-domain, which can extract the fault feature well and improve the accuracy of diagnosis [24]. Wavelet packet can be defined as the equation below:

$$\begin{cases} u_{2n}^{(j)}(t) = \sqrt{2} \sum_k h(k) u_n^{(j)}(2t - k) & n = 0, 1, \dots, m_1 \\ u_{2n+1}^{(j)}(t) = \sqrt{2} \sum_k g(k) u_n^{(j)}(2t - k) & k = 0, 1, \dots, m_2 \end{cases} \quad (4)$$

where: $u_0^{(0)}(t)$ is the scaling function $\phi(t)$, i.e., $u_0^{(0)}(t) = \phi(t)$; $u_1^{(0)}(t)$ is wavelet basis function $\psi(t)$, i.e., $u_1^{(0)}(t) = \psi(t)$; superscript (j) in the formula represents the wavelet packet basis function of level j , there will be 2^j wavelet packet bases in level j .

WPD generates time-frequency spectrum containing wavelet packet coefficients of all levels and nodes. Due to the limited frequency and time support of wavelet, the harmonic frequency is only distributed in a limited number of nodes in the WPD spectrum at each level. Once the wavelet packet basis is defined by Eq. (1), a recursive algorithm for signal decomposition can be designed to implement the wavelet packet transform. The decomposition result is given by the following formula:

$$\begin{cases} d_{j+1,2n} = \sum_m h(m - 2k) d_{j,n} \\ d_{j+1,2n+1} = \sum_m g(m - 2k) d_{j,n} \end{cases} \quad (5)$$

where, $d_{j,n}$ represents the wavelet coefficient of layer j of the n th sub-band; $d_{j+1,2n}$ and $d_{j+1,2n+1}$ represent the $j+1$ wavelet coefficients of the $2n$ sub-band and $2n+1$ sub-band respectively; m is the number of wavelet coefficients. A three-level decomposition of the WPD is shown in Fig. 1, where H represents low-pass filter and G represents band-pass filter.

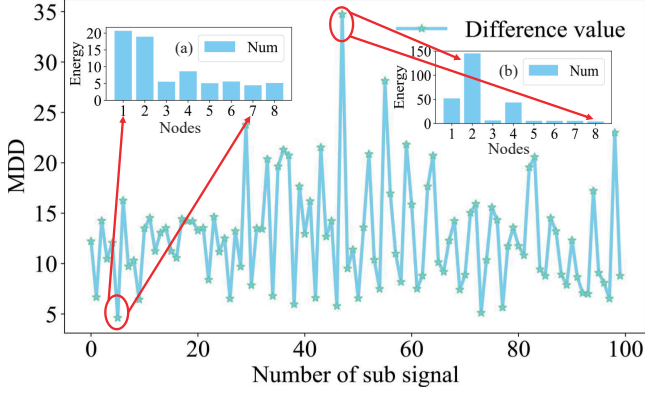


Fig. 2. MDD of 100 signal points.

B. DFSL

For a vibration signal, it can be divided into multiple sub-signals through a nonoverlapping sliding window [25]: $S_a = \{S_a^1, S_a^2, \dots, S_a^{L/s}, \dots\}$ (L is the length of S_a , s is the size of the sliding window), S in Fig. 1 represents a sub-signal $S_a^{L/s}$ in S_a . Each sub-signal will be decomposed into 8 feature sub-bands (the sub-band number is AAA, AAD, ADA, ADD...) after 3-level WPD. Each sub-band contains a set of feature coefficient matrix $d_{j+1,2n}$, $d_{j+1,2n+1}$. Use L2 norm to calculate the energy of each feature coefficient matrix. Therefore, for each sub-signal $S_a^{L/s}$, 8 energy norms can be obtained by :

$$\begin{cases} \|d_{j+1,2n}\|_2 = \left(\sum_m (h(m-2k)d_{j,n})^2 \right)^{\frac{1}{2}} \\ \|d_{j+1,2n+1}\|_2 = \left(\sum_m (g(m-2k)d_{j,n})^2 \right)^{\frac{1}{2}} \end{cases} \quad (6)$$

To obtain more stable and useful signal features, the concepts of maximum distribution difference (MDD) and discrete distribution difference (DDD) are defined. MDD refers to the ratio of the maximum and minimum energy of the sub-signal, DDD refers to the ratio of the maximum energy of all sub-bands to the energy of each sub-band. Both MDD and DDD represent the distribution difference within signals. The larger the MDD and DDD values are, the more unstable the semantic information of the signal is, that is, the greater the influence of noise on fault features. Therefore, changing the value of MDD and DDD can obtain more useful semantic information. The MDD and DDD of each sub-signal is calculated by :

$$MDD = \frac{\text{Max}(\|d_{j+1,2n}\|_2, \|d_{j+1,2n+1}\|_2)}{\text{Min}(\|d_{j+1,2n}\|_2, \|d_{j+1,2n+1}\|_2)} \quad (7)$$

$$DDD = \begin{cases} \frac{\text{Max}(\|d_{j+1,2n}\|_2, \|d_{j+1,2n+1}\|_2)}{\|d_{j+1,2n}\|_2} \\ \frac{\text{Max}(\|d_{j+1,2n}\|_2, \|d_{j+1,2n+1}\|_2)}{\|d_{j+1,2n+1}\|_2} \end{cases} \quad (8)$$

Fig. 2 shows the MDD calculation results of 100 demonstration sub-signals. The MDD value of the sub-signal in Fig. 2(a) is the coupling result of the first sub-band and the seventh sub-band, and the MDD value of this signal is 2.43, which is the minimum value in the demonstration signal. The MDD value of the sub-signal in Fig. 2(b) is the coupling result of

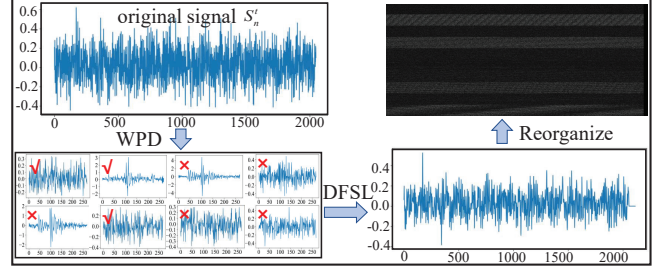


Fig. 3. Process of a signal passing through WPDRG.

the second sub-band and the eighth sub-band, and the MDD value of this signal is 34.7, which is the maximum value in the demonstration signal. This indicates that the distribution of the internal feature energy of different sub-signals is different under noise interference, and the fluctuation of the energy distribution between multiple sub-signals may be large. This may cause the fault identification model to discriminate the noise features more than the real signal features.

Based on the above analysis, for stable and accurate extraction of signal features from the influence of strong noise, a DFSL dynamic feature selection method is proposed. MDD is used to control the global feature energy distribution, while DDD is used to control the local feature energy distribution. For the different sub-bands energies of different sub-signals, the DFSL can adaptively extract the sub-bands with high and stable distribution from 8 sub-bands.

The steps of the proposed DFSL method for feature energy selection are as follows:

- 1) For a sub-signal $S_a^{L/s}$, calculate the MDD value according to Eq. (7).
- 2) Set a threshold value α for feature selection, which is considered as a hyper-parameter. The value range of MDD is effectively controlled by the value of α .
- 3) Compare MDD and α . If $MDD \leq \alpha$, select the coefficients of all sub-bands. Otherwise, go to step 4).
- 4) Calculate DDD according to Eq. (8). DDD represents the ratio of the maximum energy of all sub-bands to the energy of each sub-band. If $DDD < \alpha$, select the coefficient of the sub-band, otherwise discard the coefficient of the sub-band.

C. WPDRG

For the reconstruction of a sub-signal, based on WPD and DFSL, the WPDRG method is proposed in this paper. Algorithm 1 shows the entire process of the WPDRG method. Firstly, DFSL method is adopted to adaptively select the sub-bands of all sub-signals of S_a decomposed by WPD. Then use the selected sub-bands to reconstruct the signal, and the result of each reconstruction is shown in Eq. (9). Finally reorganize each reconstructed signal into a signal feature graph. The signal reorganization is inspired by literature [26], that is, a sub-signal $S_a^{L/s}(t)$ is divided into L/s equal parts, and each part is sequentially arranged as the line of signal image. The conversion process is shown in Eq. (10). The output I_a of the

Algorithm 1 Flow of algorithm WPDRG.

Input: Fault samples: S_a ;
 Fault type: $C = \{C_1, C_2, \dots, C_c\}$;
 Sliding window size: s ;
 Length of S_a : L
 Divide S_a : $S_a = \{S_a^1, S_a^2, \dots, S_a^{L/s}\}$;
for each $S_a^{L/s}$ in S_a :
 $S_a^{L/s} = \{x_1, x_2, \dots, x_s\}$;
Execute WPD:
 Set the wavelet packet function;
 Define the wavelet packet basis $u_{2n}^{(j)}(t), u_{2n+1}^{(j)}(t)$;
 Calculate $d_{j,n}, d_{j+1,2n}$ and $d_{j+1,2n+1}$ by recursive algorithm;
end WPD
Execute DFSL:
for each $d_{j+1,2n}$ and $d_{j+1,2n+1}$:
 Calculate $\|d_{j+1,2n}\|_2, \|d_{j+1,2n+1}\|_2$;
 Calculate MDD, DDD ;
 Set hyper-parameter α ;
if $MDD \leq \alpha$:
 select the $d_{j+1,2n}$ and $d_{j+1,2n+1}$;
else:
 if $DDD < \alpha$:
 select the $d_{j+1,2n}$ or $d_{j+1,2n+1}$;
 else:
 discard the $d_{j+1,2n}$ or $d_{j+1,2n+1}$;
 end if
end if
end for
end DFSL
 Calculate $d_{j,n}f(n)$;
 Calculate $I_a^{L/s}$;
end for
Output: $I_a = \{I_1, I_2, \dots, I_a^{L/s}\}$

algorithm contains more stable signal features and is used as input to the CNN module for depth feature extraction.

$$d_{j,n}f(n) = \sum_m h^*(m-2k)d_{j+1,2n}f + \sum_m g^*(m-2k)d_{j+1,2n+1}f \quad (9)$$

$$I = \begin{bmatrix} S_a^{L/s}(t) \dots S_a^{L/s}(t + N - 1) \\ \vdots \\ S_a^{L/s}(t + (m-1)N) \dots S_a^{L/s}(t + mN - 1) \end{bmatrix} \quad (10)$$

To better illustrate the flow of the WPDRG algorithm, Fig. 3 shows the whole process of a sub-signal going through the WPDRG transformation. Firstly, it is decomposed into eight sub-bands through WPD. Then, DFSL method is used to dynamically select the sub-bands. The selected sub-bands are used for signal reconstruction(REC), and finally reorganize(REO) the reconstructed signal. The red '✓' in the figure represents the sub-bands dynamically selected by DFSL

for signal reconstruction, while the red '✗' represents the discarded sub-bands.

D. 2D-CNN

CNN is originally used for recognition tasks of 2D signals such as images or videos [27]–[29]. The vibration signal is periodic, which means that the data in a time period is not only related to adjacent data, but also to data over several periods. Therefore, 2D-CNN can be used to identify faults from one-dimensional signals by extracting two-dimensional features of signals [30]–[32].

In this paper, each sub-signal is dynamically transformed into a feature signal graph through the WPDRG method, and these graphs are used as the input to the 2D-CNN. To implement ablation experiment, this paper sets the same network structure and parameters for all CNNs. The network structure and parameter setup of 2D-CNN are presented in TABLE I. The 2D-CNN designed in this paper consists of four convolution layer, four pooling layer, two full-connected layers and one softmax layer [33]. After passing through the first convolution layer, the reorganized signal is converted into a set of feature maps, and down-sampled through the maximum-pooling layer. This operation is repeated four times, and the results of the last sampling are sent to the full-connected layer, and then transmitted to the softmax layer through the ReLU activation function. The softmax layer selects the sparse categorical crossentropy as the loss function of the model classification. T outputs of softmax correspond to T fault states.

TABLE I
 DETAILS OF 2D-CNN

No.	Layer type	Kernel size	Channel size
1	Convolution 1	3×3	32
2	Pooling 1	2×2	32
3	Convolution 2	3×3	64
4	Pooling 2	2×2	64
5	Convolution 3	3×3	64
6	Pooling 3	2×2	64
7	Convolution 4	1×1	64
8	Pooling 4	2×2	64
9	Full-connected	100	1
10	Full-connected	10/4	1

III. FAULT IDENTIFICATION METHOD BASED ON WPDRG-2DCNN

In this section, the proposed WPDRG-2DCNN approach is described in detail and its framework is shown in Fig. 4. This method is composed of three modules, namely data preparation module, WPDRG module and 2D-CNN module.

In the data preparation module, firstly, the sensor signals of different types of faults for rotating machinery under strong noise are collected, and then the non-overlapping window method is used to split the long signal into t -segment signals. This can not only increase the amount of data required by the 2D-CNN module, but also extract more effective feature information. The t -segment signals are randomly divided into

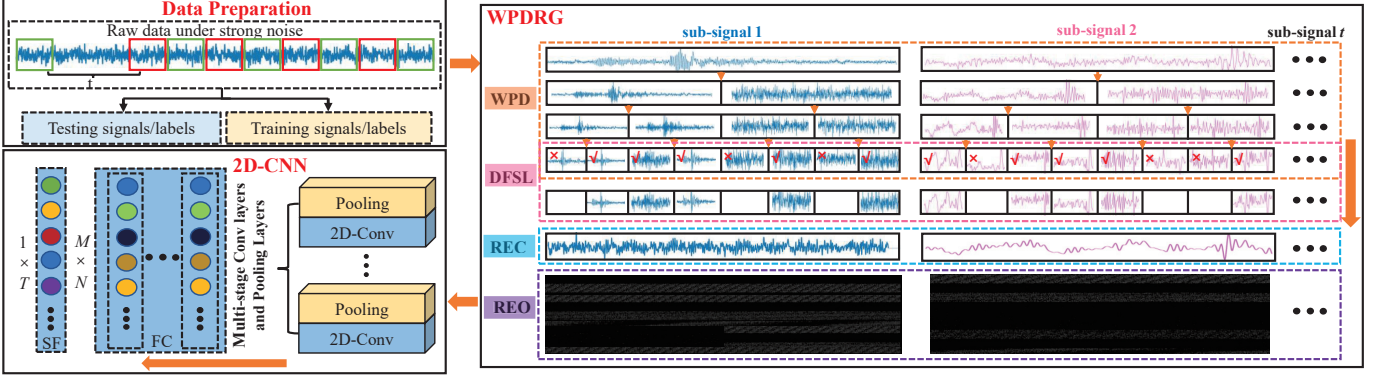


Fig. 4. Framework of WPDRG-2DCNN.

a training set and a test set according to the proportion of the number of feature types. Finally, input the prepared data into the WPDRG module to build feature signal graphs. The feature signal graphs of training set and test set are used to train and test the fault identification model respectively.

In the WPDRG module, the signal S_a will successively pass through the sub-modules WPD, DFSI, REC and REO. Due to the different sub-band energies of signals through WPD, the energy intensity distribution of each sub-signal is also different, that is, the internal features of signals are different. Then for each signal $S_a^{L/s}$, perform DFSI dynamic feature selection to adaptively select the sub-bands with high energy and MDD (or DDD) less than α . For each sub-signal, the number and position of sub-bands adaptively selected through DFSI are different. Therefore, the sub-bands with better feature intensity distribution can be selected by this method. Finally, the signal is reconstructed and reorganized according to the sub-bands selected by DFSI, and the reorganized results are sent to 2D-CNN module to extract deep features.

In the 2D-CNN module with a strong feature extraction capability, the uncertain features hidden in the reorganized signal can be automatically extracted by the convolution layer and pooling layer alternately. Finally, faults are identified through softmax layer.

The flow of fault identification using WPDRG-2DCNN is shown in Fig. 5. Before training the deep learning model, fault types need to be embedded in fault signals, and then the trained fault identification model is used to diagnose faults in collected signals. The WPDRG-2DCNN algorithm eliminates the process of manual feature extraction and realizes end-to-end intelligent information processing.

IV. EXPERIMENTS AND DISCUSSION

To verify the effectiveness and progressiveness of the proposed method, four most advanced fault diagnosis algorithms, DAMN-CNN [11], JL-CNN [12], DP-MRTN [13], CNN-LSTM [14], are compared with the method in this paper at the same time. A total of three data sets were tested, one of them was carried out on the open bearing data set, and the other two were robot grinding experiments in our laboratory.

The algorithms are run in Tensorflow2.6, with GPU GeForce RTX 3090 24G. The division ratio of training set and test

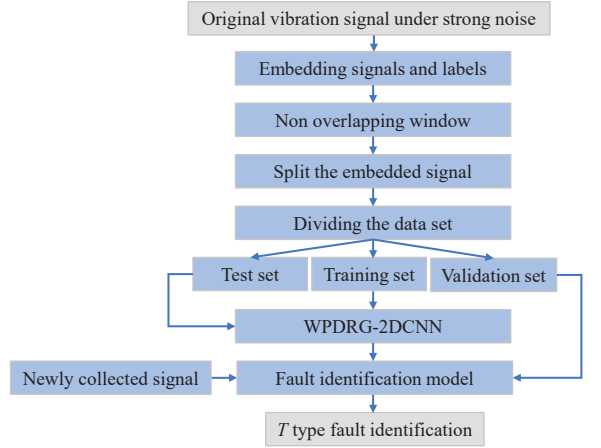


Fig. 5. Fault identification based on WPDRG-2DCNN.

set of all algorithms is 7:3. The proposed method and all the comparison methods are the optimal models determined through 10-fold cross validation. For deep learning algorithm, to reduce the randomness of the experiment, all methods were repeated 10 times. For the machine learning algorithm used for comparison, its parameter combination uses grid search to find the optimal parameter combination. In the experiment, the hyper-parameter α in the DFSI method is set to 2, that is, the maximum energy distribution difference is controlled within the proportion of 50%. The selection of α is obtained through experimental comparison. See the experimental part for details.

The evaluation index of each method is calculated according to the following formula:

$$\text{Accuracy} = \frac{TP + TN}{TP + TN + FP + FN} \quad (11)$$

for a certain type of fault, TP represents that the correct recognition signal of the classifier belongs to this fault, TN represents that the correct recognition signal of the classifier belongs to another fault, FP represents that the error recognition signal of the classifier belongs to this fault, and FN represents that the error recognition signal of the classifier belongs to another fault.

CASE 1: Fault diagnosis of bearings.

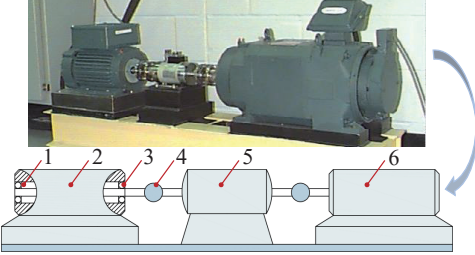


Fig. 6. CWRU bearing test rig. 1: Fan end bearing; 2: Motor; 3: Drive end bearing; 4: Coupling; 5: Torque transducer and encoder; 6: Dynamometer.

TABLE II
DATA OF FAN END BEARING

Motor load = 1 hp

Frequency(kHz)	Shaft speed(rpm)	Fault type	Fault width(in)
48	1772	IR	0.007
48	1772	IR	0.014
48	1772	IR	0.021
48	1772	OR	0.007
48	1772	OR	0.014
48	1772	OR	0.021
48	1772	BALL	0.007
48	1772	BALL	0.014
48	1772	BALL	0.021
48	1772	NORMAL	-

A. Data description and experimental preparation of CWRU test rig

To verify the effectiveness of the proposed method, we conducted experiments on a bearing firstly. The data come from the benchmark datasets of Case Western Reserve University (CWRU) [34]. The experimental platform is shown in Fig. 6. In the experiment, electrodischarge machining was used to add faults on the bearings at the motor fan end (FE). Then, install the bearing on the test bench for operation. The shaft is equipped with torque sensor and encoder. Install acceleration sensors at the fan end and drive end of the motor to collect vibration signals.

The data description is shown in TABLE II. When the sampling frequency is 48kHz, four health conditions are collected from the FE: normal condition (NORMAL), inner race fault (IR), outer race fault (OR) and ball fault (BALL). The three fault types IR, OR and BALL all contain the fault width of 0.007in, 0.014in and 0.021in. Each vibration signal in the table contains 3788800 sample points.

The benchmark datasets are relatively clean. However, the noise in industrial scenes is often a composite of noise from many different sources. If the noise is regarded as the sum of many random variables with different probability distributions, and each random variable is independent, then they will conform the Gaussian distribution. Therefore, to simulate the environment with strong industrial noise, the standard Gaussian noise is added to the dataset. The SNR is used to measure the noise intensity:

$$\text{SNR}_{\text{dB}} = 10 \lg \left(\frac{P_s}{P_n} \right) \quad (12)$$

where P_s is the signal power and P_n is the noise power.

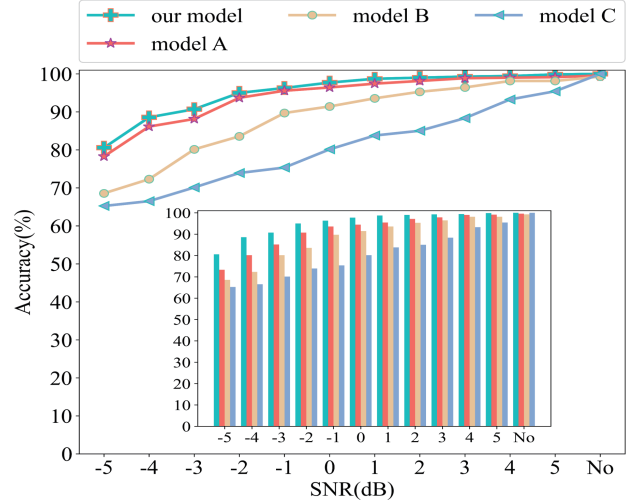


Fig. 7. Fault-diagnosis accuracy of each model in the ablation experiment. It is noted that the diagnosis performance of aforementioned 4 models are obtained under the same SNR, and the line charts of different networks are arranged separately around the corresponding SNR just to make the charts much clearer.

SNR is the signal-to-noise ratio in dB. The lower the SNR value, the greater the influence of noise on the sensor signal. In this paper, different industrial noises are simulated by the experimental conditions of $-5\text{dB} \leq \text{SNR} \leq 5\text{dB}$.

B. Experiment1: bearing of FE

The bearing model of FE is SKF deep-groove ball bearings: 6203-2RS JEM. To verify the effectiveness and superiority of the proposed method, ablation experiment was carried out firstly. The model is adjusted as follows:

- 1) Model A: Model with DFSL algorithm removed.
- 2) Model B: Model with WPDRG algorithm removed.
- 3) Model C: Replace CNN model with SVM classifier.

The model generated in the aforementioned schemes was compared with the proposed WPDRG-2DCNN, and the results are shown in Fig. 7. All models exhibit good fault diagnosis capabilities in the absence of noise. After adding noise, the comparison results with Model C show that the proposed fault diagnosis method has better fault identification ability, and the comparison results with Model B show that the proposed WPDRG reconstruction signal graph method has better anti-noise ability, and the comparison results with model A show that the proposed DFSL algorithm can further improve the accuracy of the model. This is because the graph features can be better extracted by the convolution kernel, and DFSL can make the energy contained in the graph features clearer and stable. Especially when $\text{SNR} < 4\text{dB}$, the accuracy drop gradient of the proposed method is smaller and the accuracy is higher, so the advantages of the proposed method are more obvious.

Fig. 8 shows the confusion matrix of WPDRG-2DCNN classification results under different intensity noises. A-J in the figure correspond to the 10 fault types listed in TABLE II. The number of test sets for each fault type is 70. The darker the color in the graph, the better the result of fault classification.

Fig. 8. Confusion matrix of WPDRG-2DCNN under different noise intensity. A represents BALL with 0.007in fault width; B represents BALL with 0.014in fault width; C represents BALL with 0.021in fault width; D represents IR with 0.007in fault width; E represents IR with 0.014in fault width; F represents IR with 0.021in fault width; G represents NORMAL; H represents OR with 0.007in fault width; I represents OR with 0.014in fault width; J represents OR with 0.021in fault width.

Based on all the classification results, it can be seen that the model has different ability to identify the features of different ten fault types. Thus, how to improve the imbalanced ability of model recognition is the focus of our future research.

To prove the superiority of our method, we did comparative experiments with the above four advanced methods. Fig. 9 shows the experimental results under different levels of strong noise. In the absence of noise, all methods have a fault recognition rate of 100%. With the increase of noise intensity, JL-CNN and DAMN-CNN are 0.01 and 0.02 percent higher than the methods in this paper only when $SNR = 4dB$ and $SNR = 3dB$, the methods in this paper are superior to other advanced methods under all other noise intensities. And the greater the noise intensity, the more obvious the advantages of this method. When $s = 1dB$, the accuracy of the four advanced comparison methods begin to show a large gradient decline. When the noise intensity reaches $-6dB$, the accuracy of all comparison methods fall below 80%, while ours is 83%. The experimental results show that the proposed WPDGR-2DCNN has superior fault identification capability in different levels of strong noise.

CASE 2: Fault diagnosis of robot end grinding equipment.

C. Experiment 2: grinding equipment of robot end

The grinding equipment of robot end is a typical rotating machine, which will inevitably wear out along with the grinding process, and seriously degrades the grinding quality. Therefore, the health of the grinding equipment must be monitored in the grinding process.

In this section, the fault diagnosis experiment of UR5 robot end grinding equipment will be carried out based on

the robot grinding platform in our laboratory, as shown in Figure 10. A grinder is installed at the end of the robot for grinding. Two accelerometers are installed on the end of the robot and the workpiece respectively to measure the vibration signal. Microscopes is installed at the end of the robot to measure the surface quality of the workpiece after grinding. To verify the advancement and effectiveness of the method in this paper, grinding equipment with 4 fault conditions from health to damage (F1, F2, F3, F4) are used for fault diagnosis experiments. The description of data is shown in Table III. In the experiment, the grinding tool is a plane wheel with a mesh number of 120 and the grinding trajectory is a straight line 5° from the horizontal direction. The workpiece holding, tool installation and other errors will make the weak rigid UR5 robot in the grinding operation inevitable trajectory shift, which will produce a lot of noise signals, so it is very suitable to verify the progressiveness of the proposed method.

TABLE III
DATA DESCRIPTION OF GRINDING EQUIPMENT

Frequency	10kHz
Grinding speed	5000RPM
Grinding length	50mm
Feed speed	5mm/s
Sample length	0.04s
Fault Type	F1; F2; F3; F4

Firstly, the ablation experiment was carried out under this real noise data, as shown in Fig. 11, where ACC1 and ACC2 represent the signal data collected by the accelerometer at

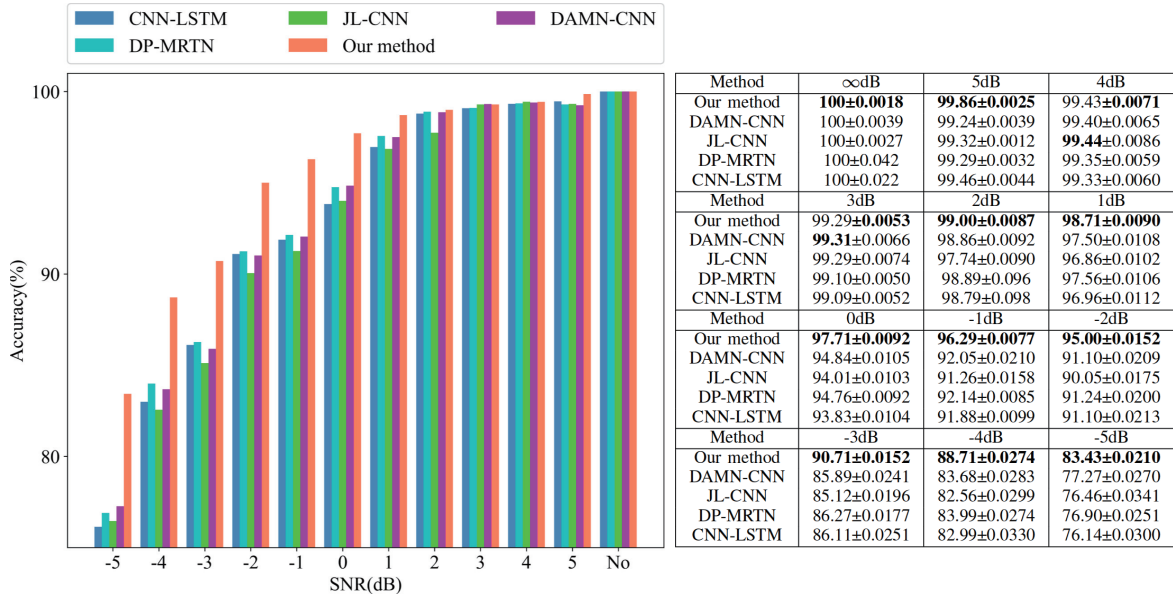


Fig. 9. Comparison results of different methods under different noise intensities.

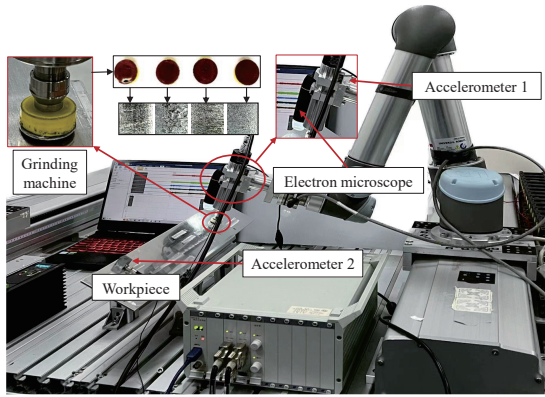


Fig. 10. Robot end grinding equipment test platform. The four grinding equipments with different fault conditions in the figure correspond to four different quality machining results.

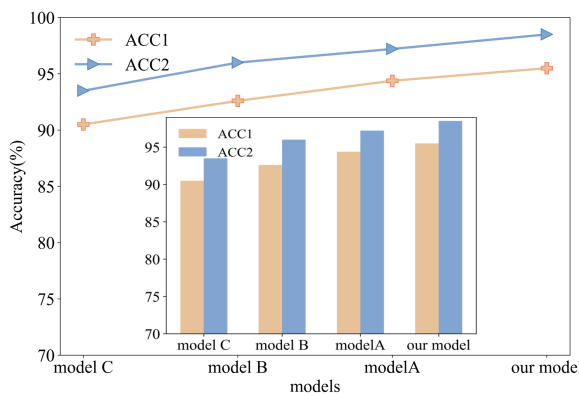


Fig. 11. Fault-diagnosis accuracy of each model in the ablation experiment.

the end of the robot and the accelerometer on the workpiece, respectively. Under the real working condition, the result of model C shows that the proposed fault diagnosis method has better fault identification ability, the result of model B

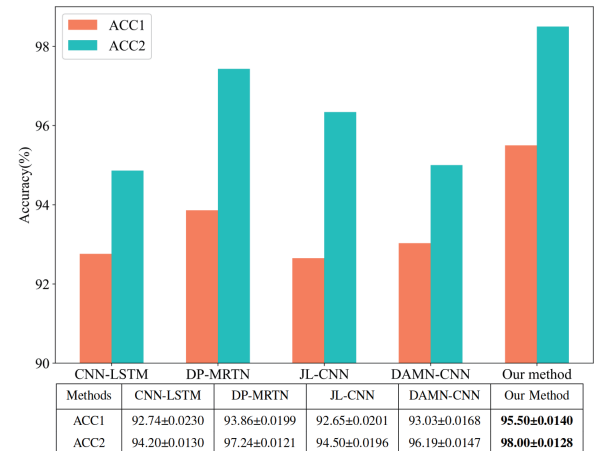


Fig. 12. Comparison results of different methods on ACC1 and ACC2.

shows that the proposed WPDRG reconstruction signal graph method has better anti-noise ability, and the result of model A shows that the proposed DFSL algorithm can further improve the accuracy of the model. Secondly, Fig. 12 shows the comparative experimental results of different fault diagnosis methods, which shows that compared with other four advanced methods, the proposed method has a better fault identification ability in actual noise signals. Fig. 13 shows the confusion matrix of five advanced methods for fault identification. It can be seen that all methods have different ability to identify different types of faults. This is caused by the unbalanced data distribution of different fault types. To sum up, the method proposed in this paper has been verified in real noise signals. **ANALYSIS OF DFSL:**

D. Experiment of feature extraction algorithm DFSL

To show the advantages of the proposed DFSL algorithm, it is compared with other feature extraction algorithms. Table

(a)CNN-LSTM				(b)DP-CNN				(c)JL-CNN				(d)DAMN-CNN				(e)Our method								
F1	44	6	0	0	F1	41	9	0	0	F1	43	7	0	0	F1	40	10	0	0 <th>F1</th> <td>44</td> <td>6</td> <td>0</td> <td>0</td>	F1	44	6	0	0
F2	3	47	0	0	F2	2	48	0	0	F2	1	48	0	1	F2	3	47	0	0 <th>F2</th> <td>3</td> <td>47</td> <td>0</td> <td>0</td>	F2	3	47	0	0
F3	0	0	47	3	F3	0	0	50	0	F3	0	0	46	4	F3	0	0	50	0 <th>F3</th> <td>0</td> <td>0</td> <td>50</td> <td>0</td>	F3	0	0	50	0
F4	0	0	3	47	F4	0	0	1	49	F4	0	0	2	48	F4	0	0	1	49	F4	0	0	0	50
F1 F2 F3 F4				F1 F2 F3 F4				F1 F2 F3 F4				F1 F2 F3 F4				F1 F2 F3 F4								
ACC1																								
(a)CNN-LSTM				(b)DP-CNN				(c)JL-CNN				(d)DAMN-CNN				(e)Our method								
F1	45	5	0	0	F1	46	4	0	0	F1	44	6	0	0	F1	45	5	0	0 <th>F1</th> <td>48</td> <td>2</td> <td>0</td> <td>0</td>	F1	48	2	0	0
F2	7	43	0	0	F2	2	48	0	0	F2	5	45	0	0	F2	3	47	0	0 <th>F2</th> <td>2</td> <td>48</td> <td>0</td> <td>0</td>	F2	2	48	0	0
F3	0	0	50	0	F3	0	0	50	0	F3	0	0	50	0	F3	0	0	50	0 <th>F3</th> <td>0</td> <td>0</td> <td>50</td> <td>0</td>	F3	0	0	50	0
F4	0	0	0	50	F4	0	0	0	50	F4	0	0	0	50	F4	0	0	0	50	F4	0	0	0	50
F1 F2 F3 F4				F1 F2 F3 F4				F1 F2 F3 F4				F1 F2 F3 F4				F1 F2 F3 F4								
ACC2																								

Fig. 13. Confusion matrix of fault identification results of different methods.

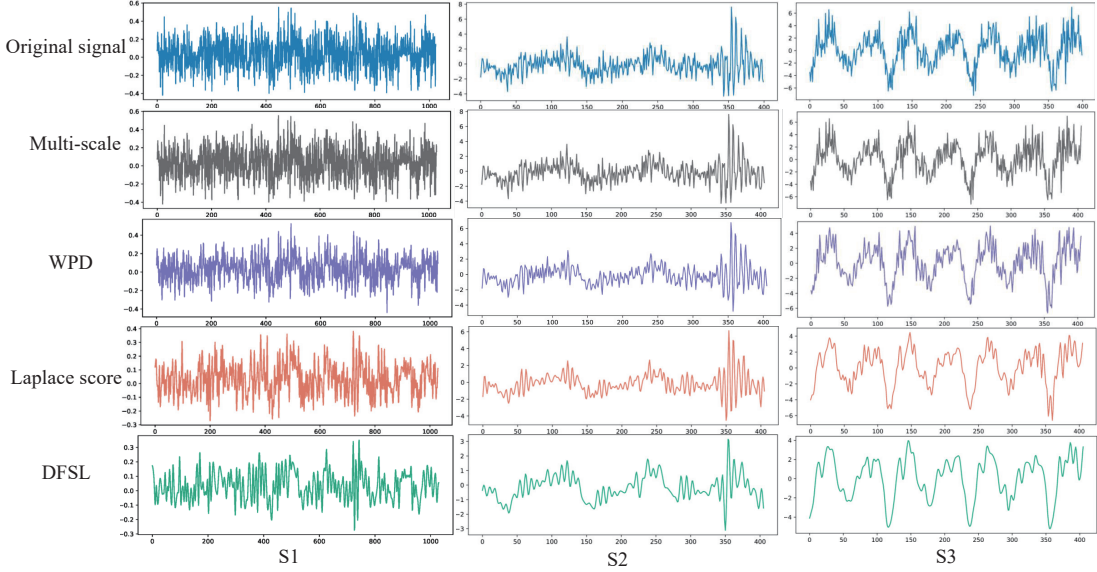


Fig. 14. Signal reconstructed by different feature extraction methods.

IV shows the comparison results of different feature extraction methods under typical neural networks and machine learning classifiers with three different datasets. In the table, FE, GE represent the fan end bearing and grinding equipment in the above experiments respectively. It can be seen that DFSL algorithm has obvious superiority. To better illustrate the progressiveness of DFSL, Fig. 14 visualizes the sub-signal segments reconstructed by three experiments using different feature extraction methods. S1, S2 and S3 represent the reconstructed signal of three different experimental data respectively. It can be seen that the signal using DFSL is smoother, so it is not easy to be interfered by noise signals, and the fault features can be better extracted.

For the selection of hyper-parameter α for DFSL, we tested different models with different hyper-parameter values under different datasets. The results of the average accuracy of the experiment are shown in Table V. The table shows that the models has the best performance when $\alpha = 2$. When the value

TABLE IV
COMPARISON BETWEEN DFSL AND OTHER FEATURE EXTRACTION METHODS

Method	DFSL	Laplace Score	WPD	Multi-scale
FE-2DCNN	97.71	96.91	96.43	93.23
FE-SVM	86.26	83.56	75.14	61.62
GE-2DCNN_ACC1	95.50	94.99	94.38	92.86
GE-SVM_ACC1	91.39	91.11	90.50	61.00
GE-2DCNN_ACC2	98.50	96.92	95.86	94.07
GE-SVM_ACC2	93.50	93.14	91.91	78.00

of α is small, the difference between the selected features is very small, and the signal is too smooth. When the value of α is large, the difference between the selected features is too large, and the normal signal may be recognized as noise. This is not conducive to the recognition of fault features.

TABLE V
COMPARISON OF DIFFERENT α VALUES

Datasets	Values of α					
	1	1.5	2	2.5	3	4
Fan End Bearing	85.20%	89.14%	92.03%	91.29%	90.05%	84.19%
Grinding Equipment_ACC1	86.76%	90.60%	93.45%	92.36%	90.73%	85.48%
Grinding Equipment_ACC2	85.76%	92.94%	96.00%	94.86%	92.90%	89.23%

V. CONCLUSION

This paper presents a new fault identification method WPDRG-2DCNN for rotating machinery under strong noise. It can directly learn features from strong noise and carry out fault identification. To improve the fault identification ability and stability of this method, the feature extraction factors (MDD and DDD) are defined. A DFSL dynamic feature adaptive extraction algorithm is developed based on MDD and DDD, which can extract important fault related sub-bands for different sub-signals based on WPD. The experimental results on a bearing and a robot grinding equipment show that DFSL has more stable feature extraction performance under strong noise conditions, which makes WPDRG-2DCNN have more stable and accurate fault diagnosis performance. This solves the problem that it is difficult to identify the fault of rotating machinery from the signal under strong noise in practical industry.

Although the proposed method has shown excellent performance in strong noise, to improve the efficiency, we set a larger experimental step for the hyper-parameter α , which may cause the optimal value of α to fall into local optimum. In addition, this paper uses the same α value for all sub-signal segments, but the characteristic distribution of each segment is different, so this may be one of the potential reasons that hinder the performance of the algorithm.

So in future research, the following work can be carried out:

- 1) The adaptive search algorithm of hyper-parameter α will be studied profoundly.
- 2) How to improve the unbalance ability of the model in fault identification of different fault types will be studied.
- 3) Vibration imaging method in fault diagnosis based on depth features of images will be explored.

REFERENCES

- [1] B. Peng, S. Wan, Y. Bi, B. Xue, and M. Zhang, "Automatic feature extraction and construction using genetic programming for rotating machinery fault diagnosis," *IEEE Transactions on Cybernetics*, vol. 51, no. 10, pp. 4909–4923, 2021.
- [2] J. Zhuang, M. Jia, Y. Ding, and X. Zhao, "Health assessment of rotating equipment with unseen conditions using adversarial domain generalization toward self-supervised regularization learning," *IEEE/ASME Transactions on Mechatronics*, vol. 27, no. 6, pp. 4675–4685, Dec. 2022.
- [3] Y. Kong, T. Wang, Z. Qin, and F. Chu, "Sparse representation classification with structured dictionary design strategy for rotating machinery fault diagnosis," *IEEE Access*, vol. 9, pp. 10 012–10 024, 2021.
- [4] J. Wang, P. Fu, S. Ji, Y. Li, and R. X. Gao, "A light weight multisensory fusion model for induction motor fault diagnosis," *IEEE/ASME Transactions on Mechatronics*, vol. 27, no. 6, pp. 4932–4941, Dec. 2022.
- [5] M. Rezamand, M. Kordestani, R. Carrieau, D. S.-K. Ting, and M. Saif, "A new hybrid fault detection method for wind turbine blades using recursive pca and wavelet-based pdf," *IEEE Sensors Journal*, vol. 20, no. 4, pp. 2023–2033, Feb. 2020.
- [6] M. Zhao, S. Zhong, X. Fu, B. Tang, S. Dong, and M. Pecht, "Deep residual networks with adaptively parametric rectifier linear units for fault diagnosis," *IEEE Transactions on Industrial Electronics*, vol. 68, no. 3, pp. 2587–2597, Mar. 2021.
- [7] B. Yang, Y. Lei, F. Jia, N. Li, and Z. Du, "A polynomial kernel induced distance metric to improve deep transfer learning for fault diagnosis of machines," *IEEE Transactions on Industrial Electronics*, vol. 67, no. 11, pp. 9747–9757, Nov. 2020.
- [8] Y. Ye, C. Huang, J. Zeng, Y. Zhou, and F. Li, "Shock detection of rotating machinery based on activated time-domain images and deep learning: An application to railway wheel flat detection," *Mechanical Systems and Signal Processing*, vol. 186, p. 109856, Mar. 2023.
- [9] H. Shao, W. Li, B. Cai, J. Wan, Y. Xiao, and S. Yan, "Dual-Threshold Attention-Guided Gan and Limited Infrared Thermal Images for Rotating Machinery Fault Diagnosis Under Speed Fluctuation," *IEEE Transactions on Industrial Informatics*, pp. 1–10, 2023.
- [10] Y. Xiao, H. Shao, S. Han, Z. Huo, and J. Wan, "Novel Joint Transfer Network for Unsupervised Bearing Fault Diagnosis From Simulation Domain to Experimental Domain," *IEEE/ASME Transactions on Mechatronics*, vol. 27, no. 6, pp. 5254–5263, Dec. 2022.
- [11] Y. Xu, X. Yan, B. Sun, and Z. Liu, "Dually attentive multiscale networks for health state recognition of rotating machinery," *Reliability Engineering & System Safety*, vol. 225, p. 108626, Sep. 2022.
- [12] H. Wang, Z. Liu, D. Peng, and Z. Cheng, "Attention-guided joint learning cnn with noise robustness for bearing fault diagnosis and vibration signal denoising," *ISA Transactions*, vol. 128, pp. 470–484, Sep. 2022.
- [13] Y. Chen, D. Zhang, H. Zhang, and Q.-G. Wang, "Dual-path mixed-domain residual threshold networks for bearing fault diagnosis," *IEEE Transactions on Industrial Electronics*, vol. 69, no. 12, pp. 13 462–13 472, Dec. 2022.
- [14] T. Huang, Q. Zhang, X. Tang, S. Zhao, and X. Lu, "A novel fault diagnosis method based on cnn and lstm and its application in fault diagnosis for complex systems," *Artificial Intelligence Review*, vol. 55, no. 2, pp. 1289–1315, Feb. 2022.
- [15] F. Husari and J. Seshadrinath, "Stator turn fault diagnosis and severity assessment in converter fed induction motor using flat diagnosis structure based on deep learning approach," *IEEE Journal of Emerging and Selected Topics in Power Electronics*, pp. 1–1, 2022.
- [16] T. Jin, C. Yan, C. Chen, Z. Yang, H. Tian, and S. Wang, "Light neural network with fewer parameters based on cnn for fault diagnosis of rotating machinery," *Measurement*, vol. 181, p. 109639, Aug. 2021.
- [17] J. Xiong, C. Li, C.-D. Wang, J. Cen, Q. Wang, and S. Wang, "Application of convolutional neural network and data preprocessing by mutual dimensionless and similar gram matrix in fault diagnosis," *IEEE Transactions on Industrial Informatics*, vol. 18, no. 2, pp. 1061–1071, 2022.
- [18] H. Shao, M. Xia, J. Wan, and C. W. de Silva, "Modified stacked autoencoder using adaptive morlet wavelet for intelligent fault diagnosis of rotating machinery," *IEEE/ASME Transactions on Mechatronics*, vol. 27, no. 1, pp. 24–33, 2022.
- [19] S. Yan, H. Shao, Y. Xiao, B. Liu, and J. Wan, "Hybrid robust convolutional autoencoder for unsupervised anomaly detection of machine tools under noises," *Robotics and Computer-Integrated Manufacturing*, vol. 79, p. 102441, Feb. 2023.
- [20] B. Peng, H. Xia, X. Lv, M. Annor-Nyarko, S. Zhu, Y. Liu, and J. Zhang, "An intelligent fault diagnosis method for rotating machinery based on data fusion and deep residual neural network," *Applied Intelligence*, vol. 52, no. 3, pp. 3051–3065, Feb. 2022.
- [21] C. Hu, Y. Wang, and J. Gu, "Cross-domain intelligent fault classification of bearings based on tensor-aligned invariant subspace learning and two-dimensional convolutional neural networks," *Knowledge-Based Systems*, vol. 209, p. 106214, Dec. 2020.
- [22] X.-B. Wang, Z.-X. Yang, and X.-A. Yan, "Novel particle swarm optimization-based variational mode decomposition method for the fault diagnosis of complex rotating machinery," *IEEE/ASME Transactions on Mechatronics*, vol. 23, no. 1, pp. 68–79, 2018.
- [23] A. Sadeghian, Z. Ye, and B. Wu, "Online detection of broken rotor bars in induction motors by wavelet packet decomposition and artificial neural networks," *IEEE Transactions on Instrumentation and Measurement*, vol. 58, no. 7, pp. 2253–2263, Jul. 2009.
- [24] Q. Hu, A. Qin, Q. Zhang, J. He, and G. Sun, "Fault diagnosis based on weighted extreme learning machine with wavelet packet decomposition and kPCA," *IEEE Sensors Journal*, vol. 18, no. 20, pp. 8472–8483, Oct. 2018.

- [25] D. Huang, W.-A. Zhang, F. Guo, W. Liu, and X. Shi, "Wavelet packet decomposition-based multiscale cnn for fault diagnosis of wind turbine gearbox," *IEEE Transactions on Cybernetics*, pp. 1–11, 2021.
- [26] W. Zhang, G. Peng, and C. Li, "Bearings fault diagnosis based on convolutional neural networks with 2-d representation of vibration signals as input," *MATEC Web of Conferences*, vol. 95, p. 13001, 2017.
- [27] D. C. Cireşan, U. Meier, L. M. Gambardella, and J. Schmidhuber, "Deep, big, simple neural nets for handwritten digit recognition," *Neural Computation*, vol. 22, no. 12, pp. 3207–3220, Dec. 2010.
- [28] D. Scherer, A. Müller, and S. Behnke, "Evaluation of pooling operations in convolutional architectures for object recognition," in *Artificial Neural Networks – ICANN 2010*, ser. Lecture Notes in Computer Science, K. Diamantaras, W. Duch, and L. S. Iliadis, Eds. Berlin, Heidelberg: Springer, 2010, pp. 92–101.
- [29] S. Kiranyaz, M.-A. Waris, I. Ahmad, R. Hamila, and M. Gabbouj, "Face segmentation in thumbnail images by data-adaptive convolutional segmentation networks," in *2016 IEEE International Conference on Image Processing (ICIP)*, Sep. 2016, pp. 2306–2310.
- [30] Z. Li, T. Zheng, W. Yang, H. Fu, and W. Wu, "A robust fault diagnosis method for rolling bearings based on deep convolutional neural network," in *2019 Prognostics and System Health Management Conference (PHM-Qingdao)*, Oct. 2019, pp. 1–6.
- [31] X. Peng, B. Zhang, and D. Gao, "Research on fault diagnosis method of rolling bearing based on 2dcnn," in *2020 Chinese Control And Decision Conference (CCDC)*, Aug. 2020, pp. 693–697.
- [32] H. Du, C. Zhang, and J. Li, "Bearing fault diagnosis based on improved residual network," in *Proceedings of IncoME-VI and TEPEN 2021*, ser. Mechanisms and Machine Science, H. Zhang, G. Feng, H. Wang, F. Gu, and J. K. Sinha, Eds. Cham: Springer International Publishing, 2023, pp. 167–184.
- [33] X. Pang, X. Xue, W. Jiang, and K. Lu, "An investigation into fault diagnosis of planetary gearboxes using a bispectrum convolutional neural network," *IEEE/ASME Transactions on Mechatronics*, vol. 26, no. 4, pp. 2027–2037, Aug. 2021.
- [34] W. A. Smith and R. B. Randall, "Rolling element bearing diagnostics using the case western reserve university data: A benchmark study," *Mechanical Systems and Signal Processing*, vol. 64–65, pp. 100–131, Dec. 2015.



Wenbin He received the B.S. degree from Process Equipment and Control Engineering, Henan University of Technology, Zhengzhou, China, in 2020. He is currently working toward the Ph.D. degree in Control Science and Engineering, Hunan University, Changsha, China.

His current research interests include mechanical fault diagnosis, robotic manufacturing, digital twin, and intelligent information processing.



Jianxu Mao received the bachelor's degree from Nanchang University, Nanchang, China, in 1993, the master's degree from the East China University of Technology, Fuzhou, China, in 1999, and the Ph.D. degree from Hunan University, Changsha, China, in 2003. He is currently an Professor and a Supervisor of doctoral students at Hunan University.

His main areas of research are intelligent information processing, computer vision, image processing, and pattern recognition.



Zhe Li (Member, IEEE) received the B.S. M.S. and Ph.D degrees from Northeastern University, Shenyang, China, in 2011, 2013 and 2018, respectively. He is now working as Associate Professor at College of Electrical and Information Engineering, Hunan University, Changsha, China. He is also a member of National Engineering Research Center of Robotic Vision and Control Technology, Hunan University, China.

His current research interests include data-driven control, intelligent industrial fault diagnosis and industrial network control systems. He is a member of the IEEE.



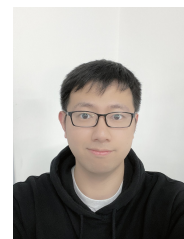
Yaonan Wang received the B.S. degree in computer engineering from East China Science and Technology University, Fuzhou, China, in 1981, and the M.S. and Ph.D. degrees in electrical engineering from Hunan University, Changsha, China, in 1990 and 1994, respectively. He was a Senior Humboldt Fellow in Germany from 1998 to 2000 and a Visiting Professor with the University of Bremen, Bremen, Germany, from 2001 to 2004. He is currently the Director of the National Engineering Research Center of Robot Visual Perception and Control Technology, Hunan University, a Professor and a Supervisor of doctoral students at the College of Electrical and Information Engineering, Hunan University, and a member of the Chinese Academy of Engineering, Beijing, China.

His research efforts mainly to robotics, intelligent information processing, intelligent control and pattern recognition.



Qiu Fang (Member, IEEE) received his PhD and BS in Control Science and Engineering from Tongji University (China) in 2017 and 2012, respectively. He has been a faculty member in the Department of Control Science and Engineering at Hunan University since 2017, where he is now an Associate Professor. He was a visiting scholar in the Department of Applied Mathematics and Statistics at the University of California, Santa Cruz, from 2015 to 2016.

His research interests focus on operational optimal control, learning methods, robotics, and their applications in the areas of green data centers and smart manufacturing. He is a member of the IEEE.



Haotian Wu received the B.S. degree in electrical engineering from Hubei University of technology, Hubei, China, in 2014 and the Ph.D. degree in control theory and control engineering from Hunan university, Hunan, China, in 2022. He is currently a Post-Doctoral Fellow with the College of Electrical and Information Engineering, Hunan University.

His current research interests include robotic 3D measurement, point clouds alignment and 3D reconstruction.